Experimental Thermal and Fluid Science 82 (2017) 83–93

Contents lists available at ScienceDirect

Experimental Thermal and Fluid Science

journal homepage: www.elsevier.com/locate/etfs

Water drop impacts on a single-layer of mesh screen membrane: Effect of water hammer pressure and advancing contact angles

Jinliang Xu *, Jian Xie, Xiaotian He, Yu Cheng, Qi Liu

The Beijing Key Laboratory of Multiphase Flow and Heat Transfer for Low Grade Energy Utilization, North China Electric Power University, 102206 Beijing, China

ARTICLE INFO

Article history:
Received 21 February 2016
Received in revised form 9 October 2016
Accepted 6 November 2016
Available online 8 November 2016

Keywords:
Drop impact
Mesh screen membrane
Water hammer pressure
Advancing contact angle
Capillary pressure

ABSTRACT

Mesh screen membrane is a functional material for gas-water or oil-water separation. If a water drop impacts on the membrane at a sufficiently high velocity, a critical condition at which daughter droplets are generated and fall down below the membrane occurs, under which the separator is failure. The objective of this paper is to determine the critical condition. Six mesh screen membranes are used. The mesh wire diameter and mesh pore are on the same-scale (10–100 μm), involving apparent cross sectional area decrease of mesh pores in the membrane depth direction. Thus, drop impacting on the membrane yields significant liquid compression in ~μs timescale to cause additional water hammer pressure. The analysis shows that the liquid compression is related to the number of mesh pores within drop project area (N). The water hammer pressure relative to dynamic pressure is found to be raised with N. The drop impacting process is governed by the dynamic pressure together with the additional water hammer pressure competed with the maximum capillary pressure at the throat location of the mesh pore. The modified Weber number $-We_w/\cos(\theta_A)$ was correlated with N in a single curve to predict the critical condition for droplet breakthrough, where We_w is characterized by the mesh pore width and $\cos(\theta_A)$ reflects the advancing contact angle effect. This paper is useful for membrane type gas-water or oil-water separator design.

1. Introduction

Metal mesh screen is a kind of functional material which is available from commercial market with acceptable cost. For example, pressure drops can be reduced when liquid flows on the modified mesh screen surface [1]. When liquid drops impact on mesh screen surface, the impingement process involves sufficiently high heat transfer coefficient [2]. The hydrophobic mesh screen can be used as a vapor-liquid separator [3]. When the two-phase mixture with liquid droplets entrained in vapor impacts on the mesh screen, vapor passes through mesh pores, but droplets cannot enter mesh pores, if the drop size is larger than the mesh pore size. Thus, the two-phases are separated and pure vapor is obtained. Recently, metal mesh screen is also proposed to be used for oil-water separation [4–6].

The drop impacting onto holes was performed by Lorenceau and Quéré [7]. They used single hole sieve of size ranging from 260 μm to 900 μm, smaller than the capillary length of $l_c = \sqrt{\sigma/\rho g}$ Z, where σ is the surface tension force, ρ is the liquid density and g is the gravity acceleration. The threshold for protruding liquid results in a balance between inertia force and capillary force using the Weber number defined as $We = \rho V^2 d/(2\sigma)$, built with the impacting velocity V, hole diameter d, surface tension σ and liquid density ρ.

Bordoloi and Longmire [8] studied the deformable drops falling through a circular orifice, having the Bond number in the range of 0.8–11. The orifice diameter is much smaller than the drop size. Effects of surface wettability were investigated. For the round edged case, a thin film of surrounding oil prevents the drop from contacting the orifice surface. Thus, the drop falling through the orifice is independent of surface wettability. For the sharp edged case, a contact is initiated at the orifice edge immediately after impacting. The surface wettability influences the drop outcome.

Few studies are reported on drop impacting onto multi holes. Brunet et al. [9] reported experiments of drop impacting on a hydrophobic micro-grid. Above a critical impacting velocity, liquid emerges to the other side to form micro droplets, having similar size of the grid holes. A method was proposed to produce a large quantity of micro-droplets. The critical Weber number is found to be much smaller than that predicted by the single hole theory [7]. The collective effect was believed to generate an additional pressure to cause easy liquid penetration. The additional pressure

* Corresponding author.
E-mail address: xjl@ncepu.edu.cn (J. Xu).

http://dx.doi.org/10.1016/j.expthermflusci.2016.11.006
0894-1777/

Nomenclature

A	flow cross section area, m^2
As	shadow area of droplet on mesh screen, m^2
Au	a unit area including a mesh pore, m^2
Bn	Bond number
C	sound speed in liquid, m/s
Ca	Capillary number
d	hole diameter, m
D	droplet diameter, m
D_c	wetting diameter, m
e_A	average deviation
e_R	mean absolute deviation
g	gravity acceleration, m/s^2
H	droplet falling height, m
ΔH	falling height variation, m
k	a constant to quantify the importance of the water hammer pressure related to the dynamic pressure (see Eq. (9))
k^*	empirical coefficient
l	wetted perimeter, m
l_c	capillary length, m
m	droplet mass, kg
N	number of mesh pores within the droplet project area (see Fig. 3 and Eq. (2))
P	pressure, Pa
Re	Reynolds number
t	time, s
Δt	time variation, s
v	droplet volume, m^3
Δv	droplet volume variation, m^3
V	impact velocity, m/s
w	mesh pore width, m
We	Weber number

Greek symbols

δ	mesh wire thickness, m
θ	dynamic contact angle, °
θ_A	advancing contact angle, °
θ_c	static contact angle, °
$\theta_{c,i}$	stable contact angle after droplet impacting, °
μ	viscosity, Pa s
ρ	density, kg/m^3
$\Delta\rho$	density variation, kg/m^3
σ	surface tension, N/m
σ_n	standard deviation

Subscript

0–3	state during drop impacting process corresponding to Fig. 10
C	capillary
D	dynamic
exp	experimental value
max	maximum
pre	predicted value
w	using the mesh pore width as characteristic length
WH	water hummer

is considered as the water hammer pressure due to the shock during a sudden change of the liquid momentum. The water hammer pressure becomes important for small holes, having the same order of the dynamical pressure.

The drop impacting on textured surfaces involves several pressure balances. The dynamic pressure $P_D = 0.5\rho V^2$ is the driving force for liquid penetration into micro structures [10]. In the initial impact stage, the contact between droplet and textured surface generates a shock wave induced water hammer pressure, which is written as $P_{WH} = k^*\rho CV$, where C is the sound speed in liquid, k^* is a empirical coefficient, having scattered values in the literature. For example, Deng et al. [11] used $k^* = 0.2$ for droplet impacting on textured solid surface. Kwon et al. [12] used $k^* = 0.003$ for microdroplet impacting on micro-pillar array. The k values did not reflect physical mechanisms of drop impacting process.

Shock wave is complicated, especially for droplet impacting onto textured microstructure. The available numerical simulations on shock waves are majorly for drops impacting on plain surface [13]. The water hammer pressure is not well understood when drops impact on micro structures. Because shock wave usually happens in μs time scale, sufficiently shorter than the heat transfer process, it generally occurs under isentropic condition. On the other hand, shock wave is caused by the liquid compression. Different drop sizes and microstructure sizes yield different water hammer pressures, it is not acceptable to use a constant k^*.

Here, we investigate the drop impacting on a single layer of mesh screen membrane. The critical condition at which daughter drop begins to occur and fall down is focused on. The driving pressure is the dynamic pressure plus the water hammer pressure. The anti-pressure is the capillary pressure, reaching maximum at the throat location of the mesh pore with the advancing contact angle. The treatment of water hammer pressure is thoroughly different from that in the literature. A k factor is defined as the water hammer pressure divided by the dynamic pressure, i.e. $k = P_{WH}/P_D$. The fundamental analysis of drop impacting obstructed by mesh wires guides us to find a key parameter of N, reflecting liquid volume change induced by compression, yielding the water hammer pressure. Our experimental data successfully correlate k as a function of N in a single curve, for all the six mesh screen pieces and different surface wettabilities. Finally, the drop breakthrough criterion is written in a non-dimensional form to have a general guideline for gas-liquid or oil-water separator design.

2. Experimental section

2.1. Fabrication and characterization of the mesh screens

Six tin bronze mesh screens with 6.15–7.79 wt% tin element are used for the experiment (see Fig. 1). They are available from the commercial market. The following procedures are performed to prepare the test sections: (1) The mesh screens with planar size of 30 mm by 30 mm were first immersed in acetone solution for 1 h to remove oil contaminations. Afterwards the pieces were rinsed by de-ionized water. (2) The mesh screens were immersed in 1 M HCl aqueous solution for 5 min to remove oxidation layer and then rinsed by de-ionized water. (3) The cleaned mesh screens were suspended in a 0.5 wt% hexane solution of 1H, 1H, 2H, 2H-per fluorodecyltriethoxysilane (CAS NO: 101947-16-4, Alfa Aesar) at room temperature for 1 h. (4) The mesh screens were drying at 110 °C for 1 h in an oven at vacuum pressure.

For comparison, the static contact angles on the solid plate (same material) without holes are measured to be 45° and 112° before and after the treatment, respectively. But the static contact

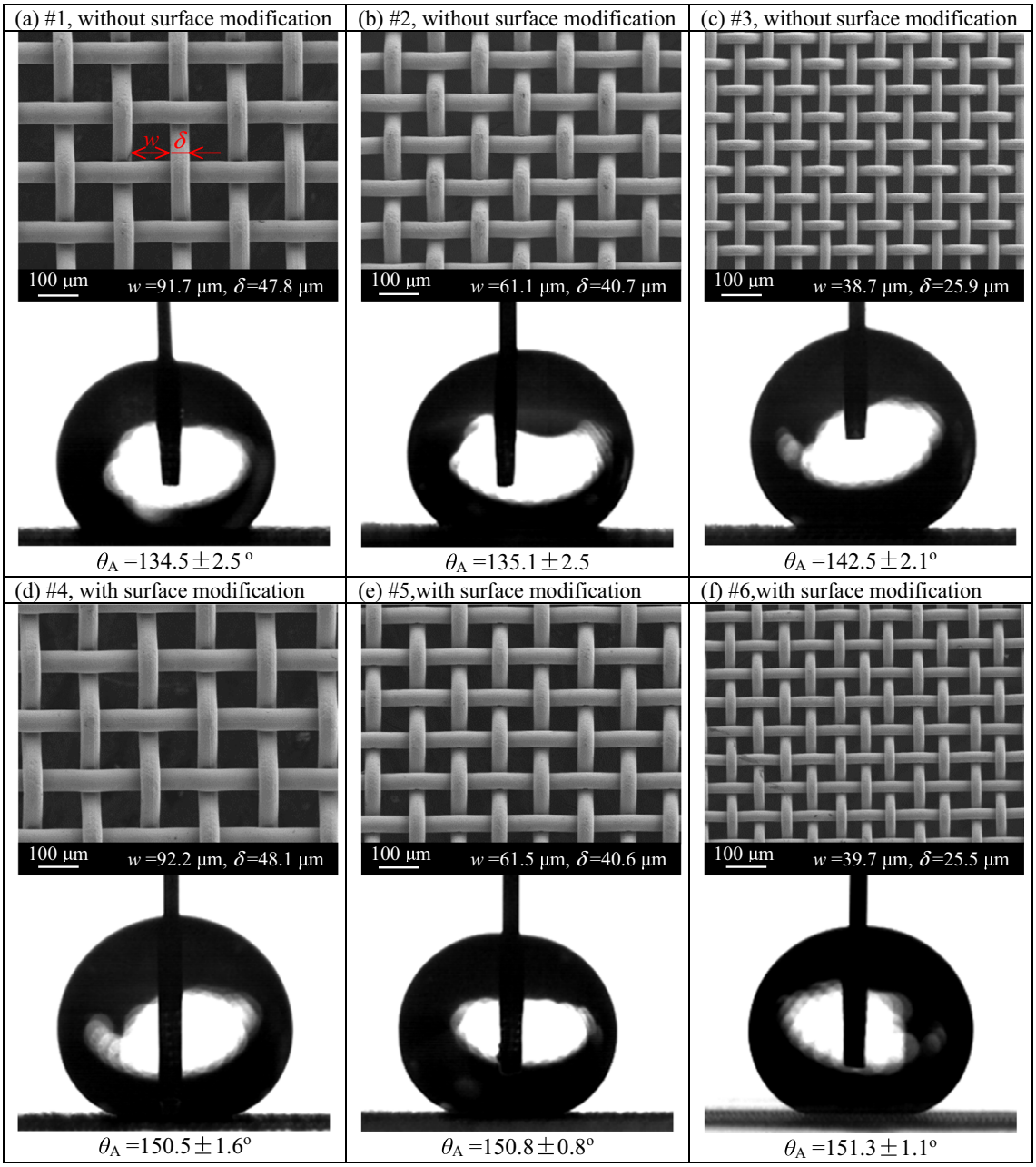

Fig. 1. The SEM photos of mesh screens and pictures for advancing contact angle measurements (Note: w, δ and θ_A are shown in each subfigure, the static contact angles θ_c are 116.9 ± 3.4°, 119.6 ± 3.6°, 125.7 ± 3.2°, 143.1 ± 3.7°, 144.0 ± 3.8°, 147.9 ± 2.6° for #1 to #6 mesh screens).

angles for mesh screens are 117–126° and 143–148° before and after treatment, respectively. The difference between the solid plate and the mesh screens is the air entrapped in mesh pores. Two groups of mesh screens were tested. The #1, #2 and #3 mesh screens (group 1) are without surface modification, having advancing contact angles of 134–142°. They follow the procedures 1, 2 and 4. The purpose of surface modification is to increase the advancing contact angles. Thus, the #4, #5 and #6 mesh screens (group 2) follow the procedures 1, 2, 3 and 4, having advancing contact angles of about 150°. Fig. 1 shows the geometry sizes of mesh screens. The mesh pore width w has the range of 39–92 μm and mesh wire thickness δ has the range of 26–48 μm. The #1 and #4, #2 and #5, and #3 and #6 almost have the identical geometry sizes, but having apparently different advancing contact angles. The advancing contact angle is an important parameter in this study. We used the dynamic sessile drop method to measure the advancing contact angle, which is similar to that used by Schmitt et al. [14]. The initial water drop has the volume of 3.5 μL (corresponding to the diameter of 1.884 mm), and the water injection flow rate is 0.5 μL/s. The needle tip has the diameter of 210 μm. Fig. 1 shows the six mesh screens, including the geometry parameters such as w and δ, the advancing contact angles θ_A. It is noted that two types of contact angles are reported in this paper: the static contact angle θ_c and the advancing contact angle θ_A (see Fig. 1). We note that the relationship between static and dynamic contact angles is important for droplet dynamics [15,16]. However, our present work focused on the advancing contact angle to establish the droplet breakthrough criterion. The relationship between static and dynamic contact angles has nothing to do with the droplet breakthrough criterion.

2.2. Experimental setup and parameter characterization

Fig. 2 shows the experimental setup. The de-ionized water droplet was generated by an injector, being one part of the OCA15 plus contact angle meter (Datephysics Instruments, Filderstadt, Germany). The injector consists of a cylinder and a needle. Several types of needles adapt the cylinder to create droplet diameters of 1.884 mm, 2.637 mm, 3.087 mm, 3.498 mm, 3.750 mm and 4.172 mm, respectively. The mesh screen with planar size of 30 mm by 30 mm was horizontally positioned on a three-dimensional object table. Thus, the mesh screen location can be precisely controlled. The droplet falling height, H, is defined as the distance between the droplet bottom and the mesh screen plane, having the range of H = 25–175 mm. Correspondingly, the impacting velocity yields $V = \sqrt{2gH}$ = 0.70–1.85 m/s. A drop falling in air environment receives drag force from the air, affecting the terminal velocity. The drag force is influenced by drop size and velocity. We compared the computed velocity of $V = \sqrt{2gH}$ with the measured one by a high speed camera. The maximum difference between them is less than 2.1%. This is because the impacting velocity (~1 m/s) is not too high. The calibration result is similar to Sen et al. [17].

The dynamic impacting process was recorded by a high speed camera (IDT, motion Pro Y4) adapting with a magnifying lens (Canon, MP-E 65 mm f/2.8 1–5X). The images are 1024 by 1024 pixels and they are taken at the frequency of 4000 frames per second. The visualization area is 17 mm by 17 mm. The resolution is 16.6 μm. The cold LED light source was used to avoid the light heating effect on the droplet.

Four non-dimensional parameters characterize the importance of one force relative to the other:

$$We_w = \frac{\rho V^2 w}{\sigma}, \quad Re_w = \frac{\rho V w}{\mu}, \quad Bn_w = \frac{\rho g w^2}{\sigma}, \quad Ca = \frac{\mu V}{\sigma} \tag{1}$$

where We, Re, Bn and Ca are the Weber number, Reynolds number, Bond number and capillary number, representing the inertia force relative to the surface tension force, inertia force relative to the viscous force, gravity force relative to the surface tension force and viscous force relative to the surface tension force, μ is the viscosity and g is the gravity acceleration. We note that the parameter characterization is different from drop impacting on solid surface [18–21]. The present study used the mesh pore width w to characterize these parameters, instead of the drop diameter. Such characterization is helpful to analyze the drop interface in mesh pores. Corresponding to the parameter ranges in this study, $Bn_w = (0.19 - 1.14) \times 10^{-3} \ll 1$ indicates the non-importance of gravity force relative to the surface tension force, Re_w = 26–170 $\gg$ 1 indicates the importance of inertia force relative to the viscous force, Ca = 0.010–0.026 shows the dominant effect of capillary force over the viscous force. However, the range of We_w = 0.254–4.335 indicates both importance of inertia force and surface tension force.

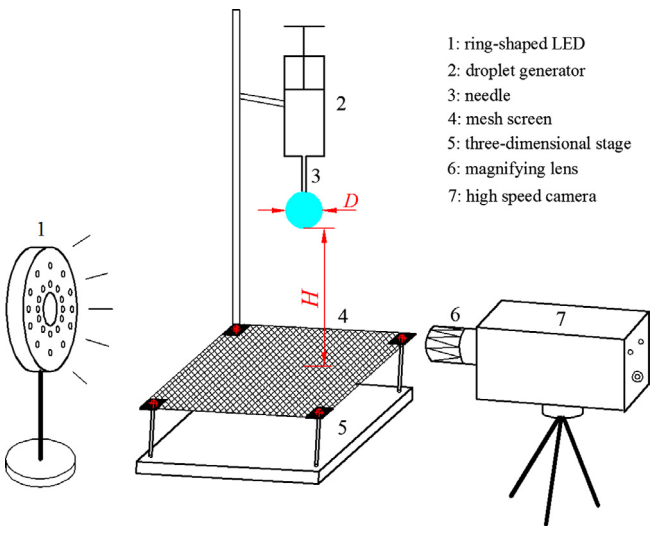

Fig. 2. The experimental setup.

The droplet size was determined by the resolution analysis of high speed images. The pixels of 1024 by 1024 corresponded to the size of 17 mm by 17 mm. Thus, the size resolution was 16.6 μm. The droplet diameter had the accuracy of 1%. The mesh screen parameters such as mesh pore width w and mesh wire thickness δ were determined by SEM images. The visualization area of 780 μm by 585 μm corresponded to the pixels of 1024 by 768. Thus, w and δ had the accuracies of 3%. The droplet falling height, H, had the uncertainty of 1 mm, having the relative accuracy of 4%. The error transmission theory yields the maximum uncertainty of 4.8% for We_w.

3. Results and discussion

3.1. Parameter N and its connection with the water hammer pressure

Fig. 3 shows a water droplet above the horizontally positioned mesh screen. The droplet has the shadow area of $A_s = \pi D^2/4$. A single mesh pore area is $A_u = (w + \delta)^2$. The parameter N is the number of mesh pores within the droplet project area:

$$N = \frac{\pi D^2}{4(w+\delta)^2} \tag{2}$$

N has the range of 142–3372. Later we will show that N is strongly related to the liquid compression for droplet impacting onto mesh holes. Thus, it is connected with the water hammer pressure.

Fig. 4 shows a unit of mesh screen. Four mesh wires are adapted each other, they are at different planes to behave three-dimensional (3D) feature. The practical unit was simplified to that shown in Fig. 4b, in which the four mesh wires are at the same plane. We note that a real 3D mesh screen is complicated to establish the connection between liquid compression and mesh screen parameter. Our two-dimensional (2D) simplification keeps the major characteristic that the top plane has the largest cross section area and the throat location has the minimum cross section area, guiding us to find the N parameter governing the liquid compression to cause water hammer pressure. Tian et al. [22] also used the 2D mesh screen to perform the force analysis when a drop is within the mesh pore.

A single mesh pore functions just like a Laval nozzle. Three cross sections are marked in Fig. 4b. The top plane $A_1B_1C_1D_1$ (red[1] color) has the largest cross section, having the rectangular width of $w + \delta$. The throat cross section $ABCD$ (blue color) has the width of w. Any other cross section has the rectangular width in between w and $w + \delta$.

We note that in this paper, the mesh wire diameter and the mesh pores are in the same scale (see Fig. 1). For #1 mesh screen, w = 91.7 μm and δ = 47.8 μm. Such configuration can be simplified as a Laval nozzle, having a top plane area of 0.0195 mm^2 and throat plane area of 0.0084 mm^2. From the top surface to the throat location, the cross sectional area is decreased by 56.8%. The significant cross sectional area decrease induces apparent liquid compression to behave shock wave. The liquid penetration is balanced by drop

[1] For interpretation of color in Fig. 4, the reader is referred to the web version of this article.

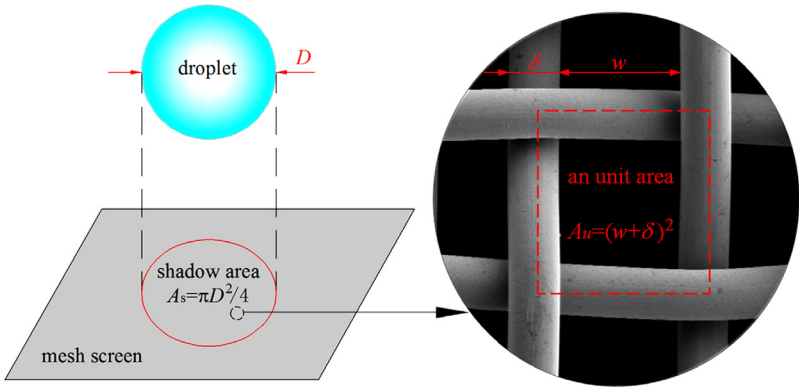

Fig. 3. The definition of *N*.

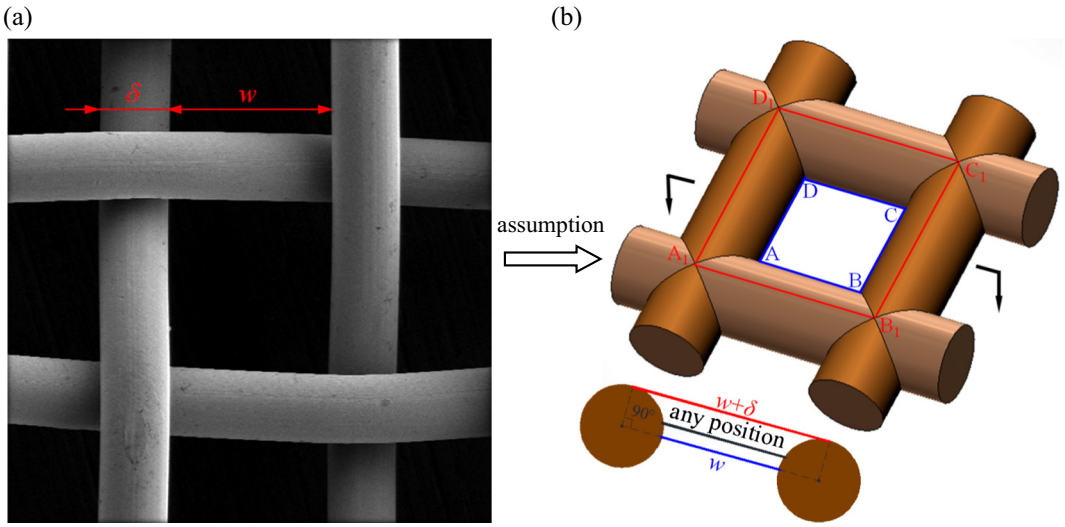

Fig. 4. The simplification of the four mesh wires to be at the same plane.

dynamic pressure and water hammer pressure competed with capillary pressure.

We estimate the time scale for a droplet impacting onto mesh pores. The impacting velocity is V and the mesh wire has the thickness of δ. The time scale for such impacting process is $t_p \sim \delta/V = 14–50$ μs. The droplet impacting process involves a shock wave induced water hammer pressure. The sound speed is defined as

$$C = \sqrt{\left(\frac{\partial P}{\partial \rho}\right)_s} \tag{3}$$

Eq. (3) yields the water hammer pressure P_{WH} as

$$P_{WH} = \Delta\rho \cdot C^2 \tag{4}$$

where $\Delta\rho$ is the liquid density change during the impacting process. The liquid density is

$$\rho = m/v \tag{5}$$

where m is the droplet mass, v is the droplet volume. We assume that m is not changed but v is changed during the fast liquid compression. The density change is

$$\Delta\rho = -\frac{m}{v^2}\Delta v \tag{6}$$

Substituting Eq. (6) into Eq. (4) yields

$$P_{WH} = -\frac{m \cdot C^2}{v^2}\Delta v \tag{7}$$

Eq. (7) shows that P_{WH} is proportion to $-\Delta v$. During the liquid compression, Δv is negative to have a positive P_{WH}.

Now we analyze the connection between P_{WH} and the parameter N. Fig. 5a shows a droplet free falling (left) and a droplet impacting onto a mesh pore (right). The liquid volume is not changed for the free falling but it is reduced due to compression by the two mesh wires. Three cases are paid attention. Fig. 5b shows the droplet impacting for ultra large droplet diameter D related to the distance between the two mesh wires, $w + \delta$. The tangent line has two contact points of A_t and B_t (the red straight line) on the top plane. The droplet has the initial contact points of A_i and B_i. The A_iB_i curvature equals to $1/D$ which is very small due to the ultra large droplet. Thus, A_iB_i approaches A_tB_t for ultra large $D/(w + \delta)$. The liquid is compressed from $A_iA_fB_fB_i$ (free falling case) to A_iABB_i due to mesh wires obstacle, in which the curve AB is the ending droplet interface. The droplet falling height is $\Delta H = V \cdot \Delta t$ between A_iB_i and the AB bottom. The traveling time Δt is on the magnitude of μs for the free falling without obstruction. The liquid compression is scaled by $D/(w + \delta)$ on the paper plane, it is also compressed by the $D/(w + \delta)$ scale perpendicular to the paper plane. Thus, the liquid volume change, $|\Delta v|$, can be scaled by $|\Delta v| \sim [D/(w + \delta)]^2$. For the case shown in Fig. 5b, $|\Delta v|$ is large and approaches maximum.

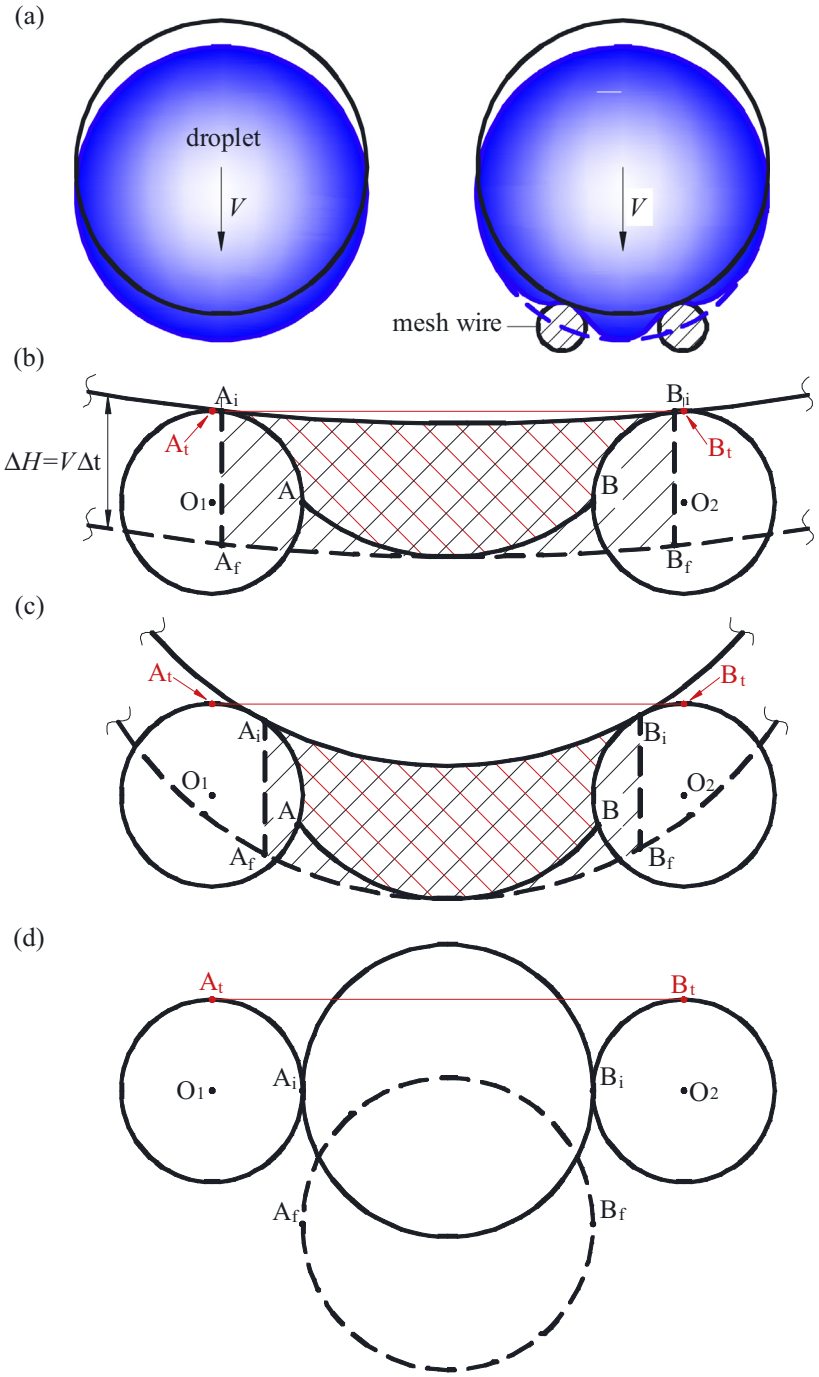

Fig. 5. The liquid compressibility degree with respect to different size ratios of drop and mesh screen (a for large N, b for moderate N and c for $N \sim 1$).

Fig. 5c shows a smaller droplet impacting compared with Fig. 5b, in which A_iB_i significantly deviates from A_iB_i. The initial contact points of A_i and B_i move towards the mesh pore throat. The liquid is compressed from $A_iA_fB_fB_i$ (free falling case) to A_iABB_i. The compression degree is decreased compared with Fig. 5b. When the droplet diameter D approaches the mesh pore width w, there is no liquid compression (see Fig. 5d), under which liquid behaves free falling without water hammer pressure.

We note that a larger drop impacting onto a smaller mesh pore is investigated here. The breakthrough criterion at which the impacting drop begins to fall down through the mesh pore was focused on. There are a large quantity of mesh pores within the drop project area, but the center hole is the weakest point for such breakthrough. Therefore, the symmetrical geometry analysis is enough to obtain the breakthrough criterion. When a smaller drop impacts on a single mesh wire or a larger mesh pore, the asymmetric impacting effect is important, such as investigated in Refs. [23,24].

In summary, Fig. 5 told us that $|\Delta v|$ or P_{WH}, strongly connects with $[D/(w+\delta)]^2$. Multiplying the factor by $\frac{\pi}{4}$ equals to N. Fig. 5b–d shows the decreased liquid compression by decreasing N. Thus, the water hammer pressure, P_{WH}, is strongly related to N. This analysis will be verified by the measurement. In our experiments, droplet heights were increased gradually until a daughter drop is seen and separated from the mother droplet below the mesh screen.

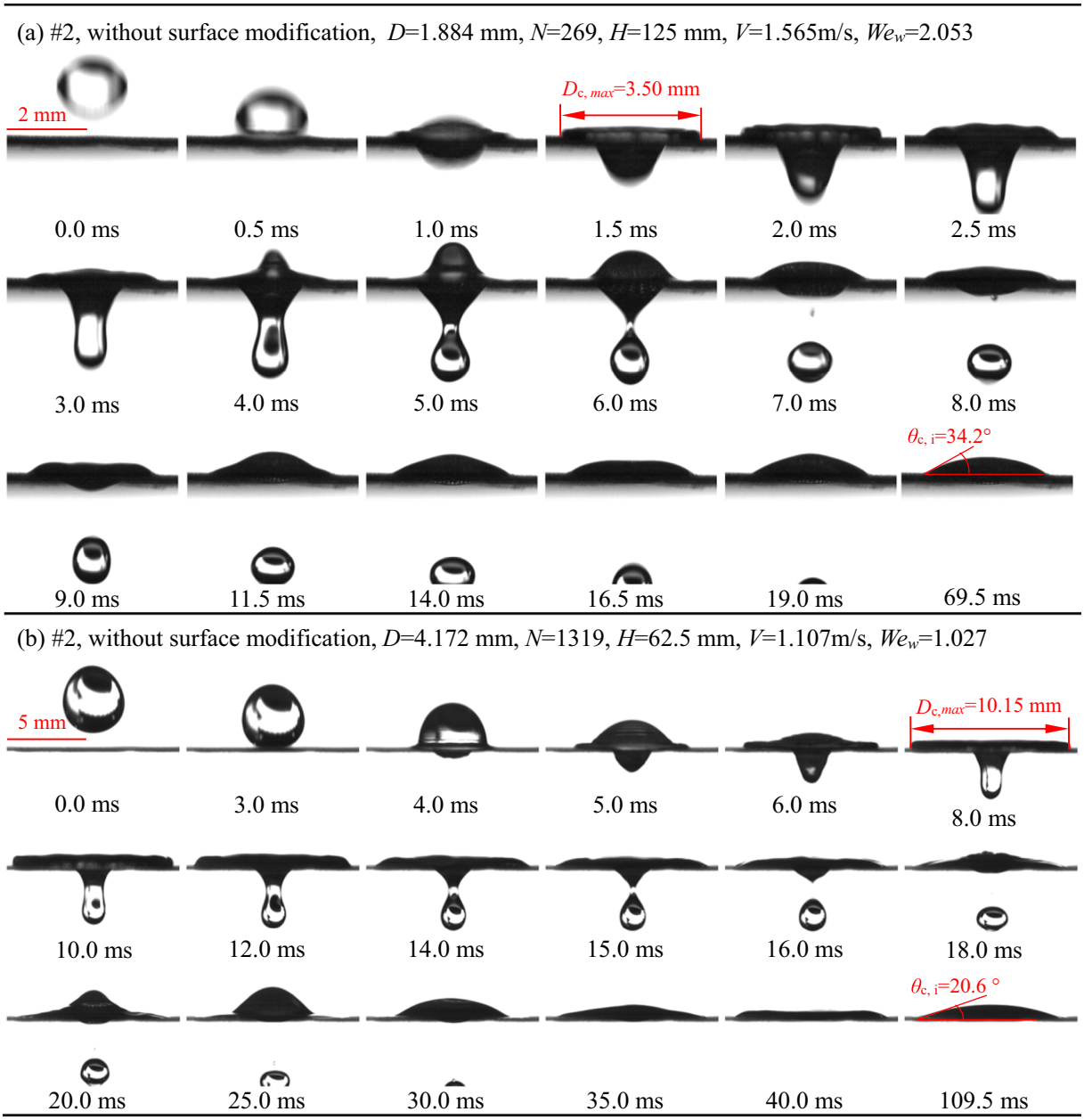

Fig. 6. Effect of N on the drop impacting process with #2 mesh screen but different drop diameters.

Fig. 6 identifies how the parameter N influences the drop impacting process. Same mesh screens are used with $w = 61$ μm and $\delta = 41$ μm, but D and N are increased from 1.884 mm and 269 in Fig. 6a to 4.172 mm and 1319 in Fig. 6b. For smaller N of 269, the drop breakthrough happens at the critical impacting velocity of $V = 1.565$ m/s ($We_w = 2.053$). The maximum wetting diameter $D_{c,max} = 3.50$ mm occurs at $t = 1.5$ ms. The neck between the mother drop and daughter drop is very thin at $t = 6.0$ ms. The daughter drop was fully separated from the mother drop and fell down at $t = 7.0$ ms. The residual liquid had a stable contact angle of 34.2° on the mesh screen (see the image at $t = 69.5$ ms in Fig. 6a). The increase of N decreases the critical impacting velocity to $V = 1.107$ m/s ($We_w = 1.027$, see Fig. 6b). The water hammer pressure, as one part of the driving pressure, is increased to lower the impacting velocity. Fig. 6 partially verified the analysis shown in Figs. 4 and 5.

3.2. Effect of advancing contact angles

Dynamic pressure and water hammer pressure are the driving pressure source. Capillary pressure is the anti-wetting pressure, which is influenced by advancing contact angle θ_A. In our experiment, θ_A was carefully measured by continuous water injection on mesh screen. All the six mesh screens were involved. Fig. 7 plots the wetting diameters D_c versus contact angles θ for #2 and #5 mesh screens. The continuous water injection yields a constant D_c but increased θ, under which the drop height is increased. A transition occurs beyond which contact angles are not changed, but D_c are increased. After the transition, the droplet is expanding on the horizontal plane, the advancing contact angle is recorded.

Fig. 8 shows the effect of θ_A on the drop impacting. Fig. 8a and b used the same droplet sizes and mesh pore sizes. Fig. 8a used the #1 mesh screen with $\theta_A = 134.5°$ but Fig. 8b used the #4 mesh

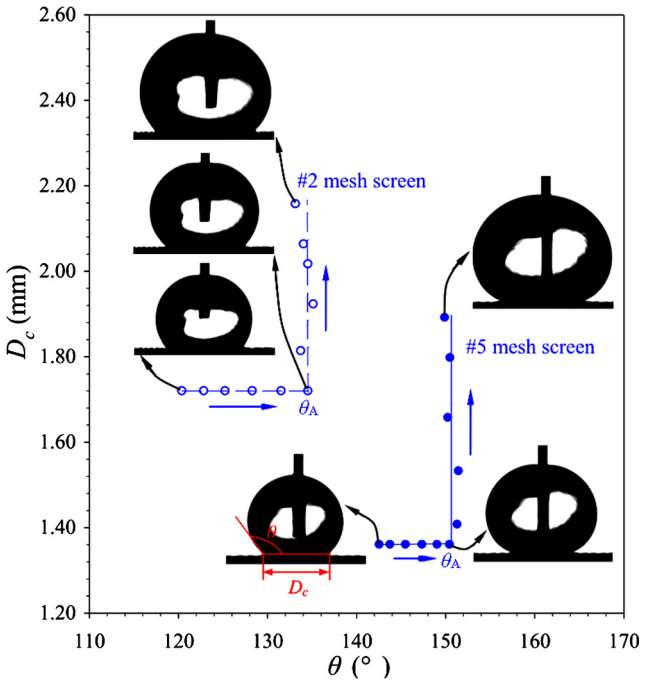

Fig. 7. The measurement of advancing contact angles on #2 and 5 mesh screens.

screen with $\theta_A = 150.5°$. The increase of θ_A increased the critical impacting velocities from $V = 1.518$ m/s in Fig. 8a to $V = 1.700$ m/s in Fig. 8b. This is due to the increased anti-wetting pressure by increasing the advancing contact angle.

3.3. Droplet breakthrough mechanism and its correlation

Holding the six mesh screens, Fig. 9 shows decreased We_w with increase of N. The We_w at $N = 100$–200 are 2.5–3.5 times of those for $N > 1000$. Larger N creates larger water hammer pressure P_{WH} to overcome the capillary pressure. The increase of advancing contact angle (θ_A) increased We_w.

This section explains the observed phenomenon. Fig. 10a shows the total wetting pressure ($P_D + P_{WH}$) versus time t, where P_D is the dynamic pressure and P_{WH} is the water hammer pressure. Fig. 10b shows the gas-liquid interface at different impacting time. The total pressure is P_D at $t = t_0$. The droplet just contacts the mesh wires at the points of A_i and B_i at $t = t_0$. Following t_0 the three-phase contact points move towards the mesh pore throat, until the throat location (points A and B) is reached at $t = t_1 < t(P_{max})$. We call the time period of $t_0 < t < t_1$ as the initial contact stage, during which the pressure is sharply increased due to the shock wave, and the advancing contact angle is not reached. A sag stage exists for $t_1 < t < t_2$, during which the three-phase contact points of A and B are stabilized at the throat location but the advancing contact angle is reached at $t = t_2$. The total wetting pressure reaches maximum at $t = t_2$. The de-pinning stage occurs for $t > t_2$ with the three-phase contact points and the gas-liquid interface move downward.

The above analysis helps us to develop a breakthrough criterion. Breakthrough occurs when the drop dynamic pressure plus the water hammer pressure exceeds the maximum capillary pressure. At the throat location, the water hammer pressure reaches maximum. The advancing contact angle is reached at the beginning of the de-pinning stage. The criterion is

$$P_D + P_{WH} \geqslant P_{C,max} \tag{8}$$

where $P_D = 0.5\rho V^2$. A k coefficient is defined to quantify the importance of the water hammer pressure related to the dynamic pressure:

$$k = \frac{P_{WH}}{P_D} = \frac{\text{water hammer pressure}}{\text{dynamic pressure}} \tag{9}$$

Thus, Eq. (8) is written as

$$(1+k)\frac{\rho V^2}{2} \geqslant P_{C,max} \tag{10}$$

Now we analyze how $P_{C,max}$ is reached. The capillary pressure in mesh pores can be written as

$$P_C = -\frac{l\sigma}{A}\cos\theta = \text{geometry effect term} \times \text{contact angle effect term} \tag{11}$$

where l is the wetted perimeter, A is the flow cross section area. The geometry effect term is $l\sigma/A = 4\sigma/w'$, where w' is the mesh pore width at any cross section in the converging section of the Laval nozzle (see Fig. 4b). The geometry effect term apparently reaches maximum at the Laval nozzle throat. The contact angle effect term is $-\cos\theta$, which also reaches maximum at the throat cross section when θ reaches θ_A at the start of the de-pinning stage (see Fig. 10).

The breakthrough criterion becomes

$$(1+k)\frac{\rho V^2}{2} \geqslant -\frac{4\sigma\cos\theta_A}{w} \tag{12}$$

Eq. (12) can be simplified as

$$-\frac{We_w}{\cos\theta_A} \geqslant \frac{8}{1+k} \tag{13}$$

Totally 36 groups of data were obtained for the critical breakthrough test. The six mesh screens have $w = 39$–92 μm, $\delta = 25$–48 μm. The #1, #2 and #3 mesh screens are without surface modifications to have $\theta_A = 134.5$–$142.5°$, while the #4, #5 and #6 mesh screens are with surface modifications to have $\theta_A = 150.5$–$151.3°$. The initial drop diameter D ranges from 1884 μm to 4172 μm. For each group of test, the measured critical impacting velocity V, mesh pore with w, drop diameter D and advancing contact angle θ_A yield a specific We_w, $\cos\theta_A$ and N. The coefficient k is computed based on Eq. (13) when equal sign is used.

Fig. 11a told us that k is well correlated as a function of N in a single curve for all the tests. The k coefficient is only connected with the size ratio of the water drop and mesh screen. The importance of water hammer pressure relative to the dynamic pressure, i.e. k, is increased when N is increased. The slopes of k with respect to N are decreased with increase of N. A limit k value is reached when N is sufficiently large. The $k \sim N$ curve is well consistent with the physical pictures shown in Figs. 5 and 10. The larger the N, the larger the liquid compression degree is, yielding larger water hammer pressure to cause the breakthrough. The k is correlated as

$$k = \frac{8}{1.1 + \frac{466}{N}} - 1 \tag{14}$$

Substituting Eq. (14) into Eq. (13) yields

$$-\frac{We_w}{\cos\theta_A} = 1.1 + \frac{466}{N} \tag{15}$$

The left side of Eq. (15) is called the modified Weber number ($-We_w/\cos\theta_A$) including the advancing contact angle effect. The right side is the N effect to influence the relative importance of the water hammer pressure with respect to the dynamic pressure. The k coefficient reaches maximum of 6.27. In other words, the water hammer pressure can be 6.27 times of the dynamic pressure when N is sufficient large such as $N > 10^4$.

Fig. 11b shows the sharp decrease of the modified Weber number with increase of N. The modified Weber number reaches a minimum value of 1.1 when N is ultra large. We compared the predicted modified Weber number (Eq. (15)) with the measured

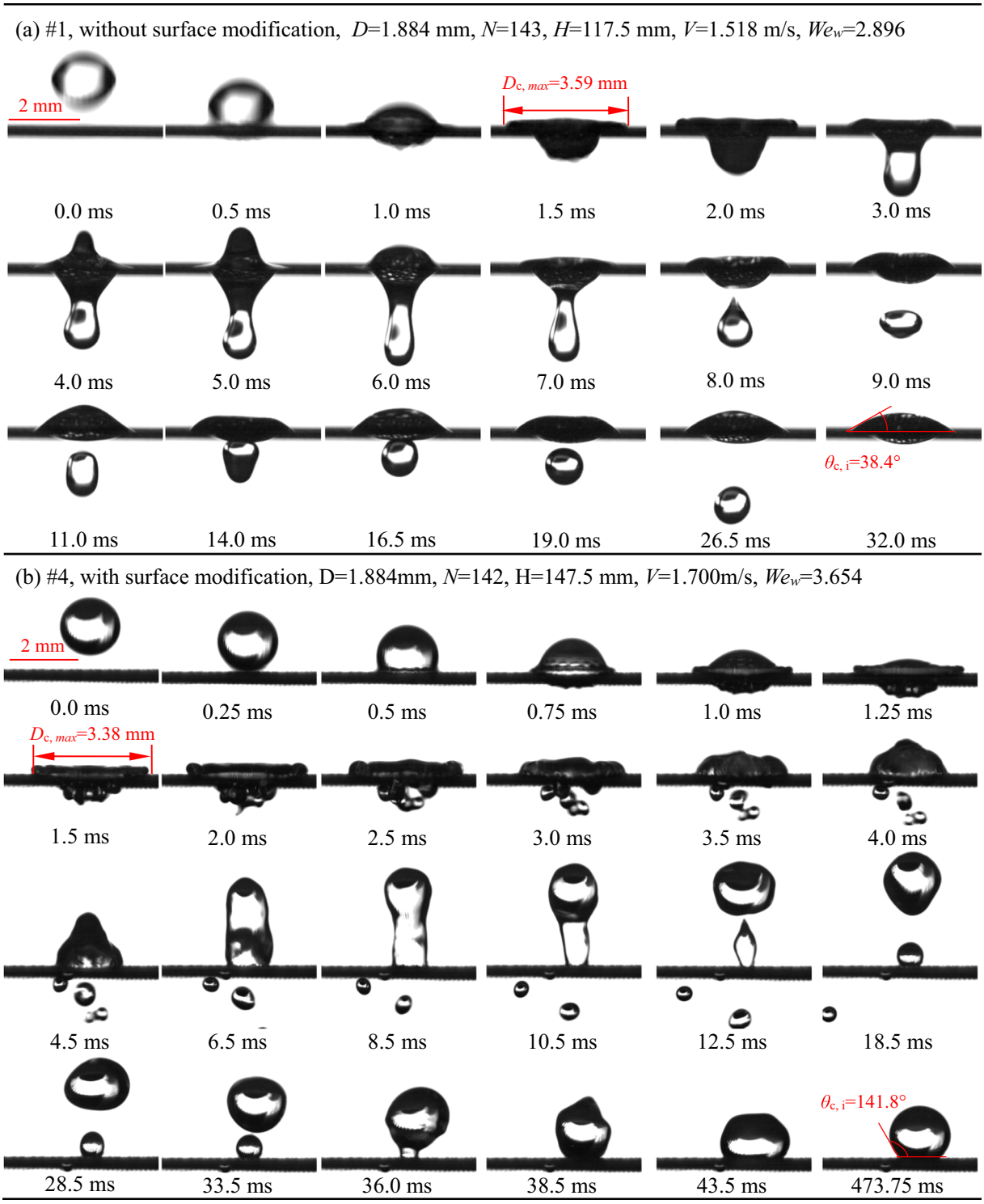

Fig. 8. The effect of advancing contact angles on the drop impacting process.

values in Fig. 11b. The subscripts of *pre* and *exp* mean the predicted value using Eq. (15) and the measured value. The agreement is perfect with the three deviation values of $e_R = 0.31\%$, $e_A = 2.79\%$ and $\sigma_n = 2.26\%$, in which e_R, e_A and σ_n mean the average deviation, mean absolute deviation and standard deviation, respectively. Their expression can be found in Ref. [25].

We summary the new finding in this paper. The geometry induced water hammer pressure, together with the dynamic pressure, are competed with the capillary pressure for the present study. This mechanism is different from the hydrodynamic focusing induced kinetic energy competed with the viscous dissipation effect for liquid penetration in Lembach et al. [26] and Sahu et al. [27]. Shock wave is a common phenomenon in nature and engineering. The first research on shock wave and water hammer pressure may be dated back to 1955, in which water drop collisions with solid surfaces was investigated [28]. Afterwards, many researchers investigated shock wave for droplets impacting on flat solid surface [29,30]. Recently, due to the development of

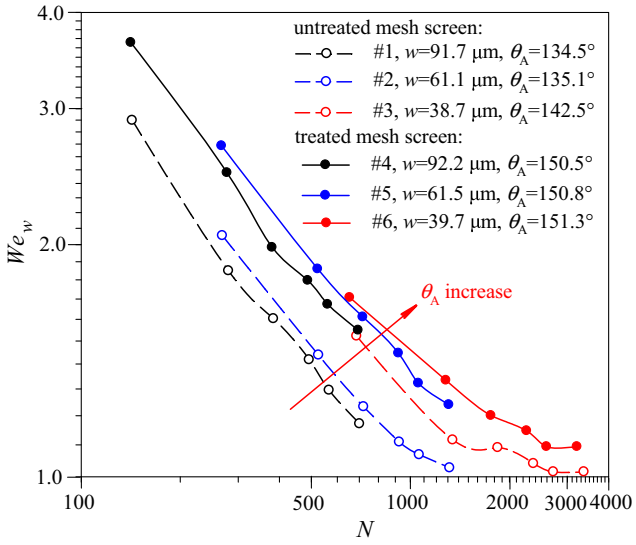

Fig. 9. Effects of N and θ_A on We_w for all the data points.

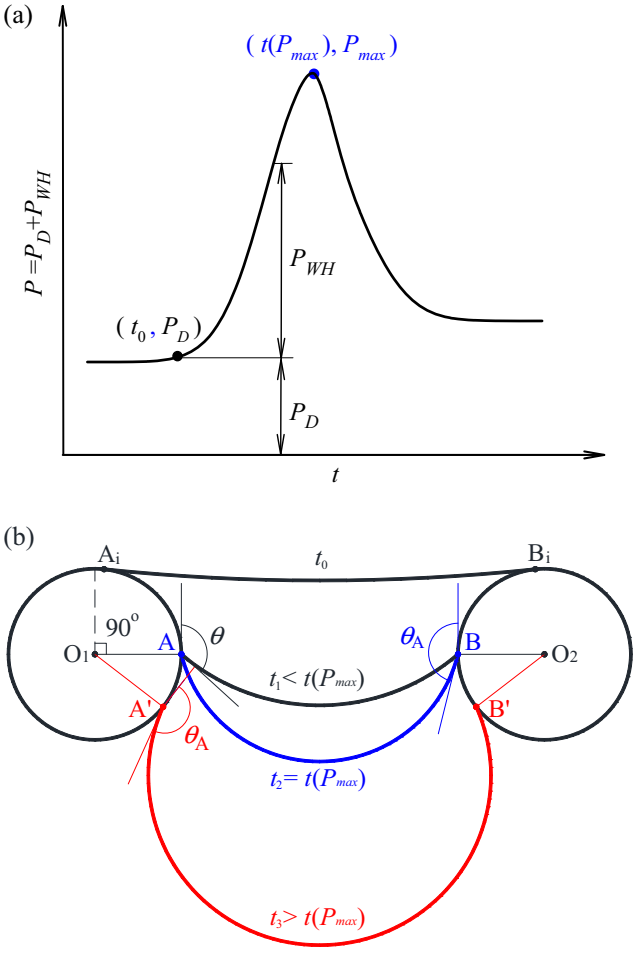

Fig. 10. The physical picture of the drop impacting within mesh pore.

micro-engineering, the drop impacting on textured surface has received great attention [31,32]. However, the water hammer pressure is fully empirically treated. The authors used $P_{WH} = k^*\rho CV$, in which the k^* coefficients are very scattered. For example, Deng et al. [11] used $k^* = 0.2$ for droplet impacting on textured solid

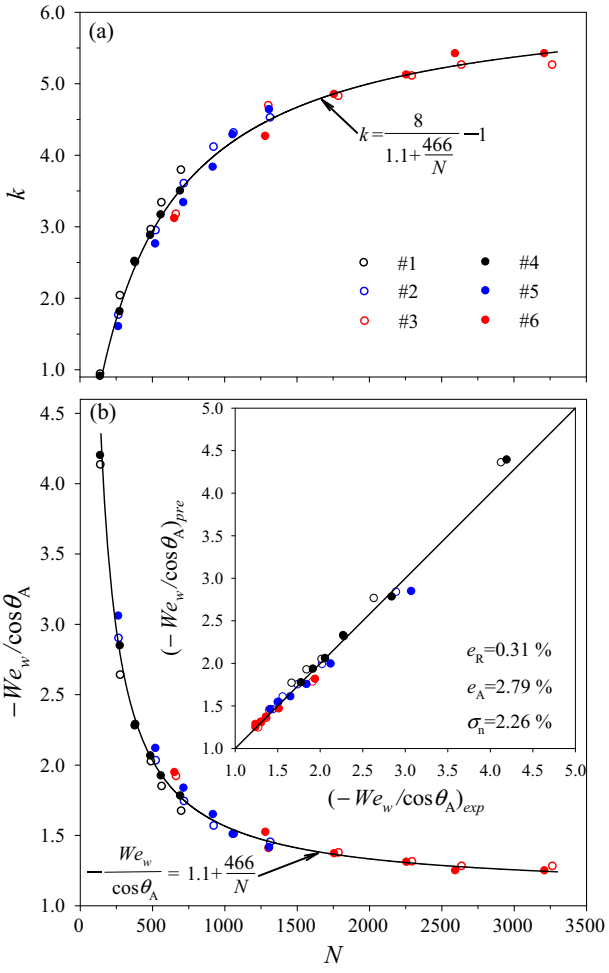

Fig. 11. The correlations of k coefficients and modified Weber number as a function of N.

surface. Kwon et al. [12] used $k^* = 0.003$ for micro-droplet impacting on micro-pillar array surface. The k^* values in these references did not consider any physical mechanism. This paper established a strong connection between the water hammer pressure and the ratio of droplet size with respect to the mesh pore size. The analysis can also be extended for droplet dynamics on other textured surfaces. Based on the physical analysis of water hammer pressure, this paper gave a criterion for droplet breakthrough on mesh screen surface (see Eq. (15)). Because the criterion is written in a non-dimensional form, it provides a general guidance to prevent the failure of oil-water or water-steam separators due to the droplet penetration.

4. Conclusions

By gradually increasing the falling heights of water drops, we obtained the critical impacting velocity at which daughter droplet appears and falls down under the mesh screen. Six mesh screens with different geometry sizes and advancing contact angles were tested with a set of drop diameters from small to large. The fundamental analysis of sound speed yields water hammer pressure versus drop volume change during drop impacting in mesh pores. The N number was defined to represent the number of mesh pores within a liquid drop projected area. The drop impacting in varied cross section mesh pore established a strong connection between the water hammer pressure and the N number. The drop

breakthrough is assumed to happen when the drop dynamic pressure plus the water hammer pressure exceeds the maximum capillary pressure, taking place at the throat location of mesh pores with the advancing contact angle. The k coefficient quantifies the importance of the water hammer pressure related to the dynamic pressure. The analysis well correlates the breakthrough criterion of $-We_w/\cos\theta_A$ as a function of N in a single curve. It is found that k is increased with N, but it reaches a limit value when N is sufficiently large, strongly supporting the sound speed analysis in converging Laval nozzle. The water hammer pressure can be several times of dynamic pressures, explaining why smaller Weber number is needed to penetrate droplet across mesh pores for large N number. This study indicates that it is not appropriate to assume a constant coefficient for water hammer pressure estimation of droplets impacting onto microstructures with different drop sizes and microstructure sizes.

Acknowledgements

This work was financially supported by the Natural Science Foundation of China (Nos. 51436004 and 51210011).

References

[1] S. Srinivasan, W. Choi, K.C. Park, S.S. Chhatre, R.E. Cohen, G.H. McKinley, Drag reduction for viscous laminar flow on spray-coated non-wetting surfaces, Soft Matter 9 (2013) 5691–5702.
[2] Z. Zhao, Y. Peles, M.K. Jensen, Water jet impingement boiling from structured-porous surfaces, Int. J. Heat Mass Transf. 63 (2013) 445–453.
[3] A.S. Al-Dughaither, A.A. Ibrahim, W.A. Al-Masry, Investigating droplet separation efficiency in wire-mesh mist eliminators in bubble column, J. Saudi. Chem. Soc. 14 (2010) 331–339.
[4] D.L. Tian, X.F. Zhang, X. Wang, J. Zhai, L. Jiang, Micro/Nanoscale hierarchical structured ZnO mesh film for separation of water and oil, Phys. Chem. Chem. Phys. 13 (2011) 14606–14610.
[5] W. Guo, Q. Zhang, H.B. Xiao, J. Xu, Q.T. Li, X.H. Pan, Z.Y. Huang, Cu mesh's super-hydrophobic and oleophobic properties with variations in gravitational pressure and surface components for oil/water separation applications, Appl. Surf. Sci. 314 (2014) 408–414.
[6] P.H. Pi, K. Hou, C.L. Zhou, X.F. Wen, S.P. Xu, J. Cheng, S.F. Wang, A novel superhydrophilic-underwater superoleophobic Cu_2S coated copper mesh for efficient oil-water separation, Mater. Lett. 182 (2016) 68–71.
[7] E. Lorenceau, D. Quéré, Drops impacting a sieve, J. Colloid Interface Sci. 263 (2003) 244–249.
[8] A.D. Bordoloi, E.K. Longmire, Drop motion through a confining orifice, J. Fluid Mech. 759 (2014) 520–545.
[9] P. Brunet, F. Lapierre, F. Zoueshtiagh, V. Thomy, A. Merlen, To grate a liquid into tiny droplets by its impact on a hydrophobic micro-grid, Appl. Phys. Lett. 95 (2009) 254102.
[10] V. Vaikuntanathan, D. Sivakumar, Transition from Cassie to impaled state during drop impact on groove-textured solid surfaces, Soft Matter 10 (2014) 2991–3002.
[11] T. Deng, K.K. Varanasi, M. Hsu, N. Bhate, C. Keimel, J. Stein, M. Blohm, Nonwetting of impinging droplets on textured surfaces, Appl. Phys. Lett. 94 (2009) 133109.
[12] D.H. Kwon, H.K. Huh, S.J. Lee, Wetting state and maximum spreading factor of microdroplets impacting on superhydrophobic textured surfaces with anisotropic arrays of pillars, Exp. Fluids 54 (2013) 1576.
[13] Q.L. Zhou, N. Li, X. Chen, T.M. Xu, S.E. Hui, D. Zhang, Analysis of water drop erosion on turbine blades based on a nonlinear liquid–solid impact model, Int. J. Impact Eng. 36 (2009) 1156–1171.
[14] M. Schmitt, J. Grub, F. Heib, Statistical contact angle analyses; "slow moving" drops on a horizontal silicon-oxide surface, J. Colloid Interface Sci. 447 (2015) 248–253.
[15] R.L. Hoffman, A Study of the advancing interface II. Theoretical prediction of the dynamic contact angle in liquid-gas systems, J. Colloid Interf. Sci. 94 (1983) 470–486.
[16] X.L. Meng, L.S. Wan, Z.K. Xu, Insights into the static and advancing water contact angles on surfaces anisotropised with aligned fibers: experiments and modeling, Colloids Surf. A: Physicochem. Eng. Asp. 389 (2011) 213–221.
[17] S. Sen, V. Vaikuntanathan, D. Sivakumar, Experimental investigation of biofuel drop impact on stainless steel surface, Exp. Therm. Fluid Sci. 54 (2014) 38–46.
[18] A.L. Yarin, Drop impact dynamics: splashing, spreading, receding, bouncing…, Annu. Rev. Fluid Mech. 38 (2006) 159–192.
[19] S.M. An, S.Y. Lee, Observation of the spreading and receding behavior of a shear-thinning liquid drop impacting on dry solid surfaces, Exp. Therm. Fluid Sci. 37 (2012) 37–45.
[20] G. Lagubeau, M.A. Fontelos, C. Josserand, A. Maurel, V. Pagneux, P. Petitjeans, Spreading dynamics of drop impacts, J. Fluid Mech. 713 (2012) 50–60.
[21] I.P. Gulyaev, O.P. Solonenko, Hollow droplets impacting onto a solid surface, Exp. Fluids 54 (2013) 1432.
[22] D.L. Tian, X.F. Zhang, J. Zhai, L. Jiang, Photocontrollable water permeation on the micro/nanoscale hierarchical structured ZnO mesh films, Langmuir 27 (2011) 4265–4270.
[23] E. Sher, L.F. Haim, I. Sher, Off-centered impact of water droplets on a thin horizontal wire, Int. J. Multiph. Flow 54 (2013) 55–60.
[24] L.S. Hung, S.C. Yao, Dripping phenomena of water droplets impacted on horizontal wire screens, Int. J. Multiph. Flow 28 (2002) 93–104.
[25] F. Xing, J.L. Xu, J. Xie, H. Liu, Z.X. Wang, X.L. Ma, Froude number dominates condensation heat transfer of R245fa in tubes: effect of inclination angles, Int. J. Multiph. Flow 71 (2015) 98–115.
[26] A.N. Lembach, H.B. Tan, I.V. Roisman, T. Gambaryan-Roisman, Y.Y. Zhang, C. Tropea, A.L. Yarin, Drop impact, spreading, splashing, and penetration into electrospun nanofiber mats, Langmuir 26 (2010) 9516–9523.
[27] R.P. Sahu, S. Sett, A.L. Yarin, B. Pourdeyhimi, Impact of aqueous suspension drops onto non-wettable porous membranes: hydrodynamic focusing and penetration of nanoparticles, Colloids Surf. A: Physicochem. Eng. Asp. 467 (2015) 31–45.
[28] O.G. Engel, Waterdrop collisions with solid surfaces, J. Res. Natl. Bur. Stand. 54 (1955) 281–298.
[29] J.E. Field, ELSI conference: invited lecture: liquid impact: theory, experiment, applications, Wear 233–235 (1999) 1–12.
[30] K.K. Haller, Y. Ventikos, D. Poulikakos, Computational study of high-speed liquid droplet impact, J. Appl. Phys. 92 (2002) 2821–2828.
[31] K. Yamamoto, H. Takezawa, S. Ogata, Droplet impact on textured surfaces composed of commercial stainless razor blades, Colloids Surf. A: Physicochem. Eng. Asp. 506 (2016) 363–370.
[32] J.B. Lee, S.H. Lee, Dynamic wetting and spreading characteristics of a liquid droplet impinging on hydrophobic textured surfaces, Langmuir 27 (2011) 6565–6573.